

Target-constrained interference-minimized approach to subpixel target detection for hyperspectral images

Hsuan Ren

Chein-I Chang, MEMBER SPIE

Remote Sensing Signal and Image
Processing Laboratory

Department of Computer Science and
Electrical Engineering

University of Maryland Baltimore County
Baltimore, Maryland 21250

Abstract. Due to significantly improved spatial and spectral resolution, hyperspectral sensors can now detect many substances that cannot be resolved by multispectral sensors. However, this comes at the price that many unknown and unidentified signal sources, referred to as interferers, may also be extracted unexpectedly. Such interferers generally produce additional noise effects on target detection and must therefore be taken into account. The problem associated with this interference is challenging because its nature is generally unknown and it cannot be identified from an image scene. This paper presents an approach, called the *target-constrained interference-minimized filter* (TCIMF), which does not require one to identify interferers, but can minimize the effects caused by interference. It designs a finite-impulse-response filter that specifies targets of interest in such a way that the desired targets and undesired targets will be passed through and rejected by the filter, respectively; the filter output energy resulting from unknown signal sources is also minimized. More precisely, the TCIMF accomplishes three tasks simultaneously: detection of the desired targets, elimination of the undesired targets, and minimization of interfering effects. A recently developed technique, constrained energy minimization (CEM), can be considered as a suboptimal version of the TCIMF. Computer simulations and hyperspectral image experiments are conducted to demonstrate advantages of the TCIMF over the CEM. © 2000 Society of Photo-Optical Instrumentation Engineers. [S0091-3286(00)02912-3]

Subject terms: classification; constrained energy minimization (CEM); target-constrained interference-minimized filter (TCIMF); subpixel detection.

Paper 990486 received Dec. 9, 1999; revised manuscript received July 24, 2000; accepted for publication July 28, 2000.

1 Introduction

Hyperspectral image analysis has increased its role in remote-sensing image processing because hyperspectral image sensors are now capable of detecting many subtle substances that usually cannot be resolved by multispectral sensors.¹ For example, two current airborne hyperspectral sensors, the 224-band AVIRIS (Airborne Visible/Infrared Imaging Spectrometer) developed by NASA's Jet Propulsion Laboratory and the 210-band HYDICE (Hyperspectral Digital Imagery Collection Experiment) developed by the Naval Research Laboratory (NRL), use 10-nm spectral resolution, as opposed to the tens of nanometers used in multispectral sensors such as SPOT and LANDSAT. However, because of their very high spectral resolution, many unknown and unidentified signal sources (referred to as *interferers* in this paper) may also be extracted unexpectedly. These interferers generally introduce additional noise effects on target detection that must be taken into account. Such phenomena have been demonstrated.²⁻⁴ A challenging problem associated with interference is that the interferers are generally unknown in nature and cannot be identified from an image scene.

Many algorithms have been developed for hyperspectral image analysis. In particular, linear mixture analysis has

been widely used for multispectral and hyperspectral image classification⁵⁻¹⁵ as well as for subpixel target detection.^{16,17} It requires a complete knowledge of the targets present in an image scene. However, in many practical applications, the nature of the interference is not known *a priori* and it must be determined directly from the scene. In Refs. 2-4 an unsupervised vector-quantization-based approach was used to find these interferers. One drawback of this approach is that it needs to know how many interferers to generate.

In order to resolve this dilemma, an alternative approach, called constrained energy minimization (CEM), was proposed,^{18,19} which does not require knowledge of the interference. Instead, it only needs to know the target to be detected. By using a specific constraint, the CEM designed a finite impulse response (FIR) filter to pass the desired target while minimizing the output energy resulting from all other signal sources. The success of the CEM in hyperspectral image processing was also demonstrated.²⁰ One disadvantage of the CEM is that if we had known there were undesired targets in an image scene (such as background signatures or other known targets), these targets could have been eliminated prior to detection rather than their energies being minimized. The CEM still considered

undesired targets along with interferers as a group of unknown signal sources; thus, instead of eliminating these undesired targets, it minimized their energies.

In this paper, we present an approach, to be called the *target-constrained interference-minimized filter* (TCIMF), which includes the CEM as a suboptimal special case. A major distinction of the TCIMF from the CEM is that the targets of interest considered in the TCIMF are divided into two classes, desired targets and undesired targets, so that the TCIMF can detect the former while eliminating the latter. This task cannot be achieved by the CEM. Furthermore, the TCIMF has the same strength as the CEM has. It does not need to identify interferers, but is still able to minimize interfering effects as does the CEM. It is derived from the concept of linearly constrained minimum variance (LCMV) proposed by Frost,²¹ which includes as a special case the minimum-variance distortionless response (MVDR), on which the CEM is based.^{22,23} Unlike the CEM, which uses a *scalar constraint* to pass only a single desired target, the TCIMF makes use of a specific *constraint vector* to pass the desired target and simultaneously annihilate the undesired targets. This idea can be traced back to oblique subspace projection^{24,25} which projects the desired signals into its range space while rejecting unwanted signals by mapping them into its null space. At the same time, the TCIMF also possesses the same strength as the CEM in minimizing the energy resulting from interference. As a result, the TCIMF accomplishes three tasks simultaneously: detection of a desired target, annihilation of the undesired targets, and minimization of interfering effects, whereas the CEM can only achieve the first and third. Accordingly, the TCIMF performs better than the CEM. From this point of view, the CEM can be viewed as a suboptimal version of the TCIMF. Experimental results show that it is indeed the case.

The remainder of this paper is organized as follows. Section 2 reviews the CEM. Section 3 presents the TCIMF approach. Section 4 conducts a comparison between the TCIMF and the CEM using a series of computer simulations and real hyperspectral data experiments. A brief conclusion is given in Sec. 5.

2 Constrained Energy Minimization

The CEM was first proposed to deal with the case that it only requires knowledge of the desired target.¹⁸ The idea arose in the MVDR beamforming approach.^{23,24} It used a linearly constrained FIR filter to pass the target to be detected through the filter while minimizing the filter output energy.

Assume that we are given a finite set of observations $\{\mathbf{r}_1, \mathbf{r}_2, \dots, \mathbf{r}_N\}$, where $\mathbf{r}_i = (r_{i1}, r_{i2}, \dots, r_{iL})^T$ for $1 \leq i \leq N$ is an L -dimensional sample pixel vector. Suppose that \mathbf{d} is the spectral signature of a target to be detected, which is assumed to be known *a priori*. The objective of the CEM is to design an FIR linear filter with L filter coefficients $\{w_1, w_2, \dots, w_L\}$, denoted by an L -dimensional vector $\mathbf{w} = (w_1, w_2, \dots, w_L)^T$, that minimizes the filter output energy subject to the following unity constraint:

$$\mathbf{d}^T \mathbf{w} = \sum_{i=1}^L d_i w_i = 1. \quad (1)$$

Now, let y_i denote the output of the designed FIR filter resulting from the input \mathbf{r}_i . Then y_i can be expressed by

$$y_i = \sum_{l=1}^L w_l r_{il} = \mathbf{w}^T \mathbf{r}_i = \mathbf{r}_i^T \mathbf{w}. \quad (2)$$

The average output energy produced by the observations $\{\mathbf{r}_1, \mathbf{r}_2, \dots, \mathbf{r}_N\}$ using the above FIR filter specified by the coefficient vector $\mathbf{w} = (w_1, w_2, \dots, w_L)^T$ is given by

$$\begin{aligned} \frac{1}{N} \sum_{i=1}^N y_i^2 &= \frac{1}{N} \sum_{i=1}^N (\mathbf{r}_i^T \mathbf{w})^T \mathbf{r}_i^T \mathbf{w} \\ &= \mathbf{w}^T \left(\frac{1}{N} \sum_{i=1}^N \mathbf{r}_i \mathbf{r}_i^T \right) \mathbf{w} = \mathbf{w}^T \mathbf{R}_{L \times L} \mathbf{w}, \end{aligned} \quad (3)$$

where $\mathbf{R}_{L \times L} = (1/N) \sum_{i=1}^N \mathbf{r}_i \mathbf{r}_i^T$ is the $L \times L$ sample autocorrelation matrix of $\{\mathbf{r}_1, \mathbf{r}_2, \dots, \mathbf{r}_N\}$. Minimizing Eq. (3) subject to the filter output response constraint $\mathbf{d}^T \mathbf{w} = \sum_{i=1}^L d_i w_i = 1$ yields

$$\min_{\mathbf{w}} \left\{ \frac{1}{N} \sum_{i=1}^N y_i^2 \right\} = \min_{\mathbf{w}} \{ \mathbf{w}^T \mathbf{R}_{L \times L} \mathbf{w} \} \quad \text{subject to} \quad \mathbf{d}^T \mathbf{w} = 1. \quad (4)$$

The solution \mathbf{w}^* to Eq. (4) has been shown to be given by¹⁸

$$\mathbf{w}^* = \frac{\mathbf{R}_{L \times L}^{-1} \mathbf{d}}{\mathbf{d}^T \mathbf{R}_{L \times L}^{-1} \mathbf{d}}. \quad (5)$$

The approach to solving Eq. (4) for the solution given by Eq. (5) was called constrained energy minimization (CEM) in Ref. 18.

3 Target-Constrained Interference-Minimized Filter

It has been demonstrated that interference plays a significant role in hyperspectral image analysis.²⁻⁴ This is primarily because hyperspectral imaging sensors can now reveal subtle materials by very fine spatial and spectral resolution. Unfortunately, this also results in extraction of unknown signal sources. In this section, an alternative approach, called the TCIMF, is developed. It assumes that an image pixel is made up of three separate signal sources: \mathbf{D} (desired targets), \mathbf{U} (undesired targets), and \mathbf{I} (interference). The idea to separate interference from a signal model as an independent source was considered in Refs. 2, 3. The CEM takes care of the interference problem by making use of a unity gain to constrain the target to be detected while minimizing the energies resulting from all other signal sources. One drawback of the CEM is that if in some cases there is some information available about \mathbf{U} , the CEM simply ignores it and treats \mathbf{U} as a part of \mathbf{I} . Obviously, this is not the best way to use information. The TCIMF resolves this problem by utilizing a constraint vector to simultaneously constrain \mathbf{D} and \mathbf{U} in such a way that it can detect the desired targets in \mathbf{D} while eliminating the undesired targets in \mathbf{U} . A similar LCMV-based approach has also been proposed to extend the CEM to detect multiple desired targets

through a constraint vector.²⁶ However, the constraint vector was used only for multiple-target detection and not for annihilation of undesired targets \mathbf{U} as done in the TCIMF to enhance the target detectability.

The idea of the TCIMF can be described as follows. Let $\mathbf{D}=[\mathbf{d}_1 \mathbf{d}_2, \dots, \mathbf{d}_p]$ and $\mathbf{U}=[\mathbf{u}_1 \mathbf{u}_2, \dots, \mathbf{u}_q]$ denote the desired-target signature matrix and the undesired-target signature matrix, respectively. A constraint vector can be derived from Eq. (1) by replacing the vector \mathbf{d} with the desired-undesired target signature matrix $[\mathbf{D} \mathbf{U}]$ and the scalar constraint 1 with the desired-undesired target signature constraint vector $[\mathbf{1}_{p \times 1}^T, \mathbf{0}_{q \times 1}^T]$ as follows:

$$[\mathbf{D} \mathbf{U}]^T \mathbf{w} = \begin{bmatrix} \mathbf{1}_{p \times 1} \\ \mathbf{0}_{q \times 1} \end{bmatrix}, \quad (6)$$

where $\mathbf{1}_{p \times 1}$ is a $p \times 1$ column vector with ones in all components, and $\mathbf{0}_{q \times 1}$ is a $q \times 1$ column constraint vector with all zeros in its components. It should be noted that in Eq. (6), $\mathbf{1}_{p \times 1}$ is used to constrain the desired targets in \mathbf{D} as was done by CEM in Eq. (4), whereas $\mathbf{0}_{q \times 1}$ is included to suppress the undesired targets $\mathbf{u}_1, \mathbf{u}_2, \dots, \mathbf{u}_q$ as was done by the oblique subspace projection.^{25,26} By taking advantage of Eq. (6), Eq. (4) can be extended to the following linearly constrained optimization problem:

$$\min_{\mathbf{w}} \{ \mathbf{w}^T \mathbf{R}_{L \times L} \mathbf{w} \} \quad \text{subject to} \quad [\mathbf{D} \mathbf{U}]^T \mathbf{w} = \begin{bmatrix} \mathbf{1}_{p \times 1} \\ \mathbf{0}_{q \times 1} \end{bmatrix} \quad (7)$$

with the optimal weight vector \mathbf{w}^* given by

$$\mathbf{w}^* = \mathbf{R}_{L \times L}^{-1} [\mathbf{D} \mathbf{U}] ([\mathbf{D} \mathbf{U}]^T \mathbf{R}_{L \times L}^{-1} [\mathbf{D} \mathbf{U}])^{-1} \begin{bmatrix} \mathbf{1}_{p \times 1} \\ \mathbf{0}_{q \times 1} \end{bmatrix}. \quad (8)$$

The FIR filter coefficient specified by \mathbf{w}^* given above is called the TCIMF.

4 Experimental Results

In this section, we conduct a comparison between the CEM and the TCIMF, using a series of computer simulations and real hyperspectral data experiments, to demonstrate the superior performance of the TCIMF.

4.1 Computer Simulations

A laboratory AVIRIS data set considered in Ref. 27 was used for performance evaluation. The data set contained the five field reflectance spectra—blackbrush, creosote leaves, dry grass, red soil, and sagebrush—shown in Fig. 1 with spectral coverage from 0.4 to 2.5 μm . There were 158 bands after water bands and bands with low signal-to-noise ratio (SNR) were removed.

In this example, the three signatures, blackbrush, creosote leaves, and sagebrush, were used as targets of interest, red soil as a background signature, and dry grass as an interferer. A set of 300 mixed pixels were simulated. Each simulated pixel contained one background signature, which is red soil with abundance fixed at 5%, and one interferer, which is dry grass with abundance fixed at 5%. In addition, each pixel also contained two undesired target signatures: creosote leaves and sagebrush, with evenly split abundance,

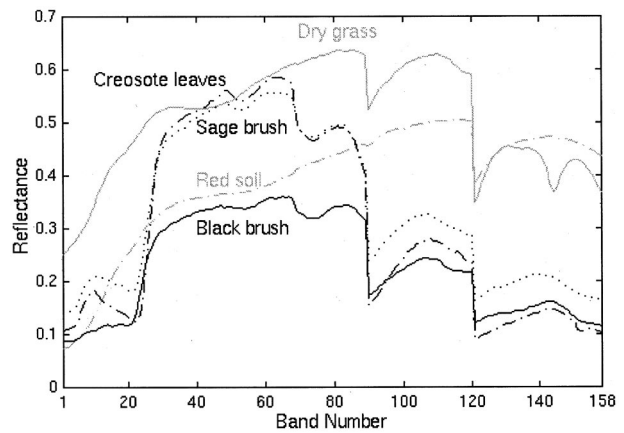


Fig. 1 Spectral signatures of five AVIRIS lab data: blackbrush, creosote leaves, dry grass, red soil, and sagebrush.

45%. Now at pixels 50, 100, 150, 200, 250, 300 we added the desired target signature, blackbrush with abundance 5%, 10%, 20%, 40%, 60%, 80%, respectively, while evenly reducing the abundance fractions of the two undesired target signatures, creosote leaves and sagebrush. For example, pixel 50 contained 5% blackbrush as the desired target signature, 42.5% creosote leaves and 42.5% sagebrush as undesired target signatures, 5% dry grass as an interferer, and 5% red soil as a background signature. The abundance fractions of five signatures in these 300 simulated mixed pixels are shown in Fig. 2. In addition, a white Gaussian noise was added to each pixel to achieve 30:1 SNR, which was defined as 50% reflectance divided by the standard deviation of the noise.¹⁸ Using blackbrush as the desired signature \mathbf{d} , three variants of the TCIMF were implemented, depending upon how the undesired-signature matrix \mathbf{U} was selected. One variant used the two undesired signatures, creosote leaves and sagebrush, to make up the undesired-

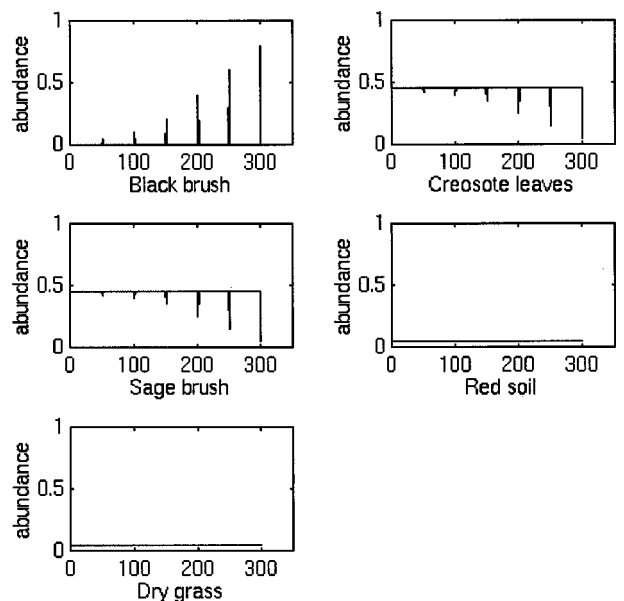


Fig. 2 Abundance allocation of 300 simulated pixels. The abscissa gives the pixel number.

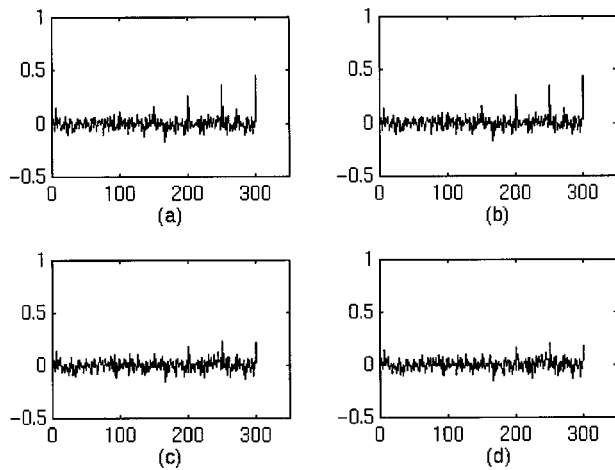


Fig. 3 Results in detecting blackbrush: (a) TCIMF with $\mathbf{U} = [\text{creosote leaves, sagebrush}]$; (b) TCIMF with $\mathbf{U} = [\text{blackbrush}]$; (c) TCIMF with $\mathbf{U} = [\text{sagebrush}]$; (d) CEM.

signature matrix \mathbf{U} , with the constraint vector chosen to be $(1,0,0)^T$, while the other two used only one undesired signature to form \mathbf{U} , with the constraint vector given by $(1,0)^T$. Figures 3(a)–3(c) show the respective detection results, and Fig. 3(d) shows the detection results of the CEM with blackbrush as the desired signature \mathbf{d} while discarding creosote leaves and sagebrush. As we can see from Fig. 3(a), the TCIMF detected target pixels 150 (barely detected), 200, 250, 300, but missed target pixels 50, 100. Then the performance of the TCIMF was slightly degraded as shown in Figs. 3(b) and 3(c), where only one signature used for \mathbf{U} . The performance of CEM in Fig. 3(d) was the worst: it missed all of the six target pixels. This experiment demonstrates the significance of constraining the undesired-target-signature matrix \mathbf{U} to zero in addition to minimizing the energy contributed from \mathbf{U} .

Similar computer simulations to those done for Fig. 2 were also conducted with using creosote leaves as the desired target signature and $\mathbf{U} = [\text{blackbrush, sagebrush}]$ as the undesired targets. The detection results are shown in Fig. 4. Interestingly, in this case the detection performance of the full TCIMF was only slightly better than that of the CEM and of the TCIMF with \mathbf{U} using only one undesired target signature, while the detection performance in the latter three cases was nearly the same, as shown in Figs. 4(b) to 4(d), where the CEM detected creosote leaves at pixels 200, 250, and 300. However, when the same simulations were conducted using sagebrush as the desired target signature and $\mathbf{U} = [\text{blackbrush, creosote leaves}]$ as the undesired target signatures, the detection results, shown in Fig. 5, are very different from those in Figs. 3 and 4. In this case, the full TCIMF and the TCIMF using $\mathbf{U} = [\text{creosote leaves}]$ performed nearly the same by extracting sagebrush at pixels 200, 250, and 300, and significantly better than the CEM and the TCIMF using only blackbrush as the undesired target signature. The detection performance of the TCIMF with $\mathbf{U} = [\text{blackbrush}]$ was close to that of the CEM and they all missed the first five targets at pixels 50, 100, 150, 200, and 250. However, comparing Fig. 5(b) to Fig. 5(d), the former performed slightly better

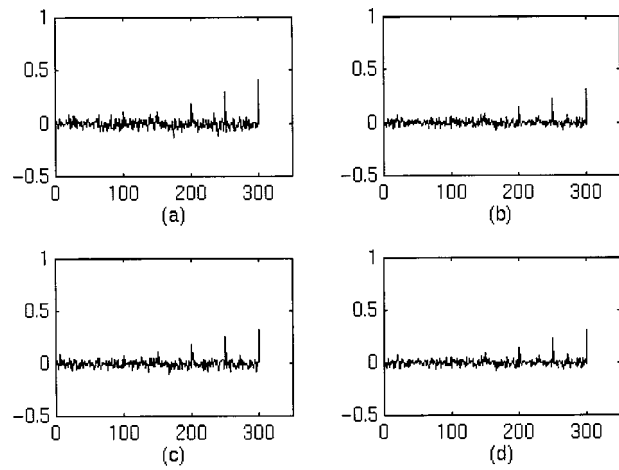


Fig. 4 Results in detecting creosote leaves: (a) TCIMF with $\mathbf{U} = [\text{blackbrush, sagebrush}]$; (b) TCIMF with $\mathbf{U} = [\text{blackbrush}]$; (c) TCIMF with $\mathbf{U} = [\text{sagebrush}]$; (d) CEM.

than the latter (i.e. the CEM) in detection of sagebrush, where the sagebrush pixel 3000 was barely detected.

All these phenomena can be explained by examining the spectral signatures of the five targets in Fig. 1 and measuring their spectral similarity by spectral information divergence (SID),^{4,28–31} which can be defined as follows. Assume that two pixel vectors are given by $\mathbf{r}_1 = (r_{11}, r_{12}, \dots, r_{1L})^T$ and $\mathbf{r}_2 = (r_{21}, r_{22}, \dots, r_{2L})^T$ with $r_{ij} \geq 0$. Normalizing \mathbf{r}_1 and \mathbf{r}_2 to unity yields two probability vectors $\mathbf{p}_1 = (p_{11}, p_{12}, \dots, p_{1L})^T$ and $\mathbf{p}_2 = (p_{21}, p_{22}, \dots, p_{2L})^T$, respectively, where $p_{ij} = r_{ij} / \sum_{j=1}^L r_{ij}$ for $i = 1, 2$ and $j = 1, 2, \dots, L$. Then the SID between \mathbf{r}_1 and \mathbf{r}_2 is defined as the Kullback-Leibler information divergence³² between \mathbf{p}_1 and \mathbf{p}_2 ,

$$\text{SID}(\mathbf{r}_1, \mathbf{r}_2) = \sum_{j=1}^L p_{1j} \log \frac{p_{1j}}{p_{2j}} + \sum_{j=1}^L p_{2j} \log \frac{p_{2j}}{p_{1j}}. \quad (9)$$

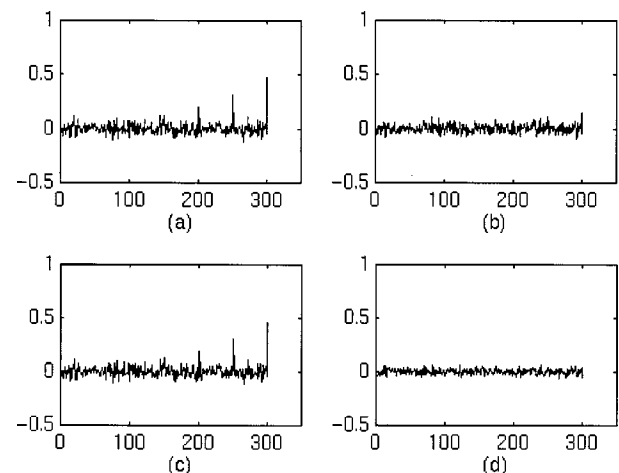


Fig. 5 Results in detecting sagebrush: (a) TCIMF with $\mathbf{U} = [\text{creosote leaves, sagebrush}]$; (b) TCIMF with $\mathbf{U} = [\text{blackbrush}]$; (c) TCIMF with $\mathbf{U} = [\text{creosote leaves}]$; (d) CEM.

Table 1 Spectral similarity values measured by SID among the five signatures in Fig. 1.

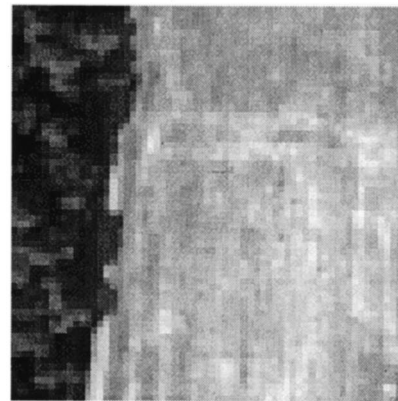
	Black brush	Creosote leaves	Dry grass	Red soil	Sage brush
Black brush	0	0.0497	0.0766	0.1861	0.0063
Creosote leaves		0	0.2298	0.4154	0.0303
Dry grass			0	0.0640	0.0973
Red soil				0	0.2340
Sage brush					0

For more details, we refer to Ref. 31.

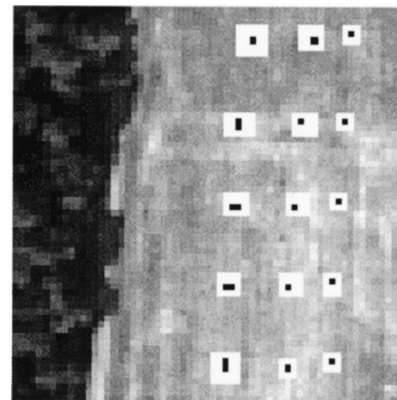
Table 1 tabulates the SID-generated spectral similarity values reproduced from Refs. 30, 31; the smaller the value, the more similar the two signatures. It shows that blackbrush and sagebrush had the most similar spectral signatures, with the spectral similarity value as small as 0.0063, compared to the spectral similarity values 0.0497 between blackbrush and creosote leaves, and 0.0303 between creosote leaves and sagebrush.^{30,31} Because the spectral similarity value between blackbrush and sagebrush is so small, it was very difficult to differentiate one from the other. Therefore, if one was used as the desired target signature and the other as the undesired target signature, most of the spectral abundance of the desired target signature was eliminated by the TCIMF or minimized by CEM. As a result, the detection performance was significantly reduced, as shown in Figs. 3(c) and 3(d) as well as Figs. 5(b) and 5(d).

4.2 Hyperspectral Image Experiments

The data used in this example were HYDICE data after geometric correction. The low-signal, high-noise bands (bands 1 to 3 and bands 202 to 210) and the water-vapor absorption bands (bands 101 to 112 and bands 137 to 153) have been removed. Figure 6(a) shows a HYDICE image scene of size 64×64 (band 30), and Fig. 6(b) provides the exact locations of 15 targets of interest in the scene, where the black pixels indicate the target center pixels and the pixels in the white masks are considered to be target pixels mixed with background pixels. These 15 target panels are located on the right field and arranged in a 5×3 matrix. Each element in this matrix is a square panel and denoted by p_{ij} with row indexed by $i=1, \dots, 5$ and column indexed by $j=a, b, c$. For each row $i=1, \dots, 5$, the three panels p_{ia}, p_{ib}, p_{ic} were made by the same material but have three different sizes. For each column $j=a, b, c$, the five panels $p_{1j}, p_{2j}, p_{3j}, p_{4j}, p_{5j}$ have the same size but were made from five different materials. The sizes of the panels in the first, second, and third columns are $3 \text{ m} \times 3 \text{ m}$, $2 \text{ m} \times 2 \text{ m}$, and $1 \text{ m} \times 1 \text{ m}$, respectively. So the 15 panels have five different materials and three different sizes. The ground truth of the image scene provides the precise spatial coordinates of these 15 panels. The 1.5-m spatial resolution of the image scene suggests that except for $p_{1a}, p_{2a}, p_{3a}, p_{4a}, p_{5a}$, which are two-pixel panels, all the panels are only one pixel wide. From Fig. 6(a), none of these panels is visible. Apparently, without ground truth



(a)



(b)

Fig. 6 (a) A band-30 HYDICE image scene. (b) Spatial locations of 15 panels in (a).

provided by Fig. 6(b) there is no way to locate these panels in the scene. Figure 7 plots the five panel spectral signatures in Fig. 6(b), where the i th panel signature P_i was obtained by averaging the panel center pixels in row i . Table 2 tabulates the SID similarity values of the five panel

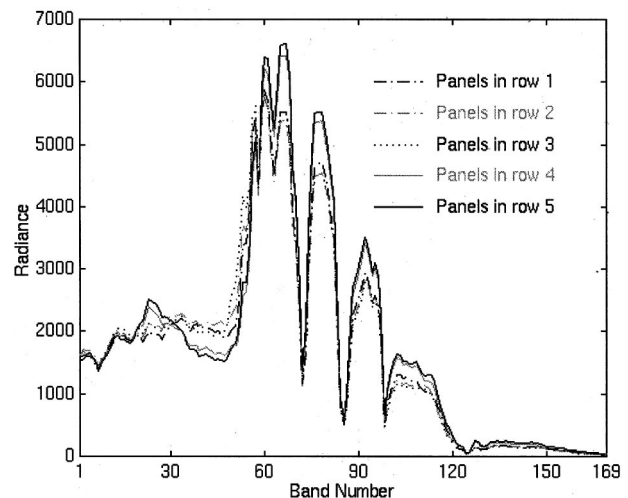


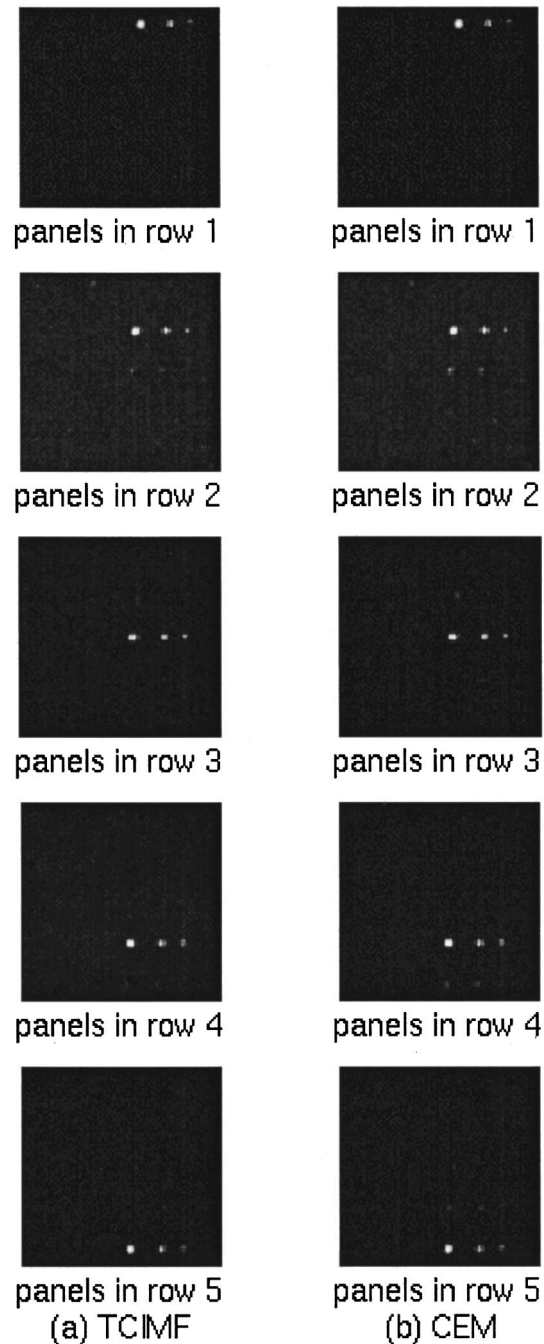
Fig. 7 Plot of the five panel spectral signatures in Fig. 6(b).

Table 2 Spectral similarity values measured by SID among the five signatures in Fig. 6.

Panels in row	1	2	3	4	5
1	0	0.0027	0.0060	0.0161	0.0217
2		0	0.0023	0.0267	0.0336
3			0	0.0330	0.0395
4				0	0.0017
5					0

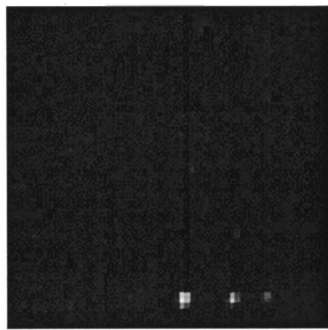
signatures, P_1 , P_2 , P_3 , P_4 , P_5 , in Fig. 7. When the CEM was implemented, the panel to be detected was designated as the desired target while discarding all the information of other target panels. By contrast, the TCIMF not only used the knowledge of the target panels to be detected to pass the desired target panels, but also used the knowledge of undesired target panels to eliminate them. The detection results of the TCIMF and CEM are shown in Figs. 8(a) and 8(b), respectively. According to Fig. 7 and Table 2, the spectral signatures of panels in rows 4 and 5 are very similar: their spectral similarity value measured by the SID was 0.0017. As expected, CEM detected the panels in one row and also picked up a few panel pixels in another row. A similar phenomenon was also observed in the detection of panels in rows 2 and 3, because the spectral signatures of panels in rows 2 and 3 are also very similar, with SID-measured spectral similarity value 0.0023. By contrast, the TCIMF performed better than CEM in nulling such undesired panel pixels. Although the SID-measured similarity value between P_1 and P_2 , 0.0027, is comparable to the value 0.0023 between P_2 and P_3 , the SID-measured similarity value between P_1 and P_3 , 0.0060, is almost three times the value between P_1 and P_2 . In addition, the spectral shape of P_1 is not as close to the spectral shapes of P_2 and P_3 as they are to each other. As a result, the TCIMF and the CEM performed equally well in detecting panel pixels in row 1. This experiment demonstrates that the SID similarity values and the geometric shapes of spectral signatures have significant effects on target detection performance.

In order to see how the TCIMF performed using different panels as undesired target signatures, Figs. 9(a) to 9(c) show the results of detecting panels in row 5 with \mathbf{U} made up of panels in row 4, panels in rows 3 and 4, and panels in rows 2 to 4, respectively. The results shown in Figs. 9(a) to 9(c) are very close. The reason is that all the \mathbf{U} used contained the panels in row 4 and removed their interfering effects to enhance the detection of the panels in row 5. Whether or not the panels in other rows were included in \mathbf{U} had very little effect on the detection performance, since their spectral signatures were different from those of the panels in row 5. However, if the panels in row 4 were not included in \mathbf{U} , the detectability for the panels in row 5 was reduced to that of the CEM, as shown in Figs. 10(a) to 10(c) using $\mathbf{U}=[\text{row } 3]$, $\mathbf{U}=[\text{row } 2, \text{row } 3]$, and $\mathbf{U}=[\text{row } 1, \text{row } 2, \text{row } 3]$, respectively, where the panels in row 4 are still barely visible, as in Fig. 8(b), and could not be nulled out as was done in Fig. 8(a) and Figs. 9(a) to 9(c) by the TCIMF that included the panels in row 4 in \mathbf{U} .

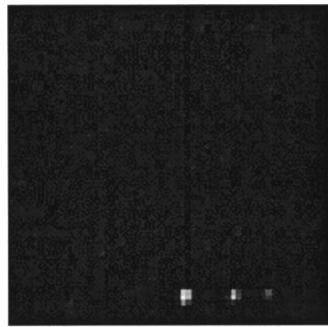
**Fig. 8** Results in detecting the 15 panels: (a) TCIMF; (b) CEM.

5 Conclusion

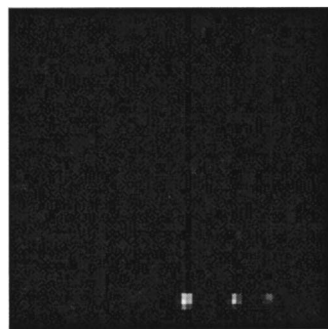
A target-constrained interference-minimization approach is presented in this paper. It takes advantage of the strengths of the CEM while mitigating its disadvantages. It divides targets of interest into a class of desired targets and another class of undesired targets, while considering interference as a separate signal source. With this three-component signal-source model, a target-constrained interference-minimized filter (TCIMF) can be designed to achieve detection of desired targets, annihilation of undesired targets, and minimi-



(a)



(b)



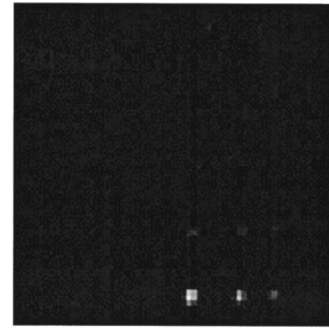
(c)

Fig. 9 Results on the TCIMF in detecting three panels in row 5: (a) $\mathbf{U}=[\text{row } 4]$; (b) $\mathbf{U}=[\text{row } 3, \text{row } 4]$; (c) $\mathbf{U}=[\text{row } 2, \text{row } 3, \text{row } 4]$.

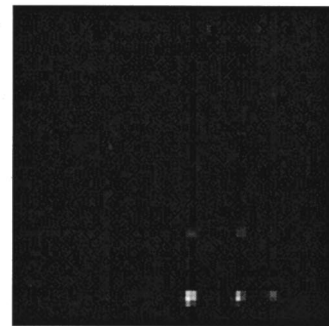
zation of interfering effects in a single operation. It improves the CEM in that the effects of undesired targets are minimized by the TCIMF rather than being eliminated by the CEM.

It should be noted that in order to make a fair comparison between the TCIMF and the CEM, only a single target was used for experiments, since the CEM could detect only one target at a time. However, in order for the CEM to be used as a classifier, it must be implemented multiple times to classify different targets. In contrast with the CEM, the TCIMF requires only one implementation to detect and classify multiple different targets in the same manner as the LCMV proposed in Ref. 21.

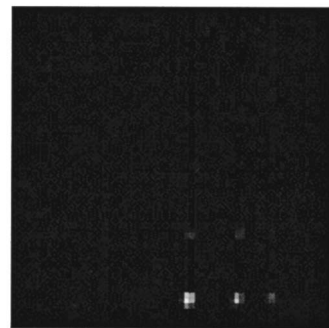
As seen in Fig. 6(a), without ground truth, obtaining information on targets to be detected is extremely difficult. Under this circumstance, developing an unsupervised CEM and TCIMF without appealing to ground truth is highly desirable. Several unsupervised learning methods currently



(a)



(b)



(c)

Fig. 10 Results on the TCIMF in detecting three panels in row 5: (a) $\mathbf{U}=[\text{row } 3]$; (b) $\mathbf{U}=[\text{row } 2, \text{row } 3]$; (c) $\mathbf{U}=[\text{row } 1, \text{row } 2, \text{row } 3]$.

being investigated^{2,4,33,34} can be used for this purpose.

It is also worth noting that the CEM and the TCIMF are very sensitive to the target information used in their implementation.³⁴

Acknowledgment

The authors would like to thank Bechtel Nevada Corporation for support under contract No. DE-AC08-96NV11718 through the Department of Energy and for the AVIRIS data provided by Dr. J. C. Harsanyi. The authors are particularly grateful for an anonymous reviewer's constructive comments, which greatly improved the presentation.

References

1. G. Vane and A. F. H. Goetz, "Terrestrial imaging spectroscopy," *Remote Sens. Environ.* **24**, 1–29 (1988).
2. C.-I. Chang, T. L. Sun, and M. L. G. Althouse, "An unsupervised

interference rejection approach to target detection and classification for hyperspectral imagery," *Opt. Eng.* **37**, 735–743 (1998).

3. C.-I Chang and Q. Du, "Interference and noise adjusted principal components analysis," *IEEE Trans. Geosci. Remote Sens.* **37**, 2387–2396 (1999).
4. C. Brumbley and C.-I Chang, "An unsupervised vector quantization-based target signature subspace projection approach to classification and detection in unknown background," *Pattern Recogn.* **32**, 1161–1174 (1999).
5. R. A. Schowengerdt, *Remote Sensing: Models and Methods for Image Processing*, 2nd ed., Academic Press, New York (1997).
6. M. O. Smith, J. B. Adams, and D. E. Sabol, "Spectral mixture analysis—new strategies for the analysis of multispectral data," in *Image Spectroscopy—a Tool for Environmental Observations*, J. Hill and J. Mergier, Eds., pp. 125–143, ECSC, EEC, EAEC, Brussels and Luxembourg (1994).
7. J. B. Adams, M. O. Smith, and A. R. Gillespie, "Image spectroscopy: interpretation based on spectral mixture analysis," in *Remote Geochemical Analysis: Elemental and Mineralogical Composition*, C. M. Pieters and P. A. Englert, Eds., pp. 145–166, Cambridge University Press (1993).
8. A. R. Gillespie, M. O. Smith, J. B. Adams, S. C. Willis, A. F. Fischer, III, and D. E. Sabol, "Interpretation of residual images: spectral mixture analysis of AVIRIS images, Owens Valley, California," in *Proc. 2nd AVIRIS Workshop*, pp. 243–270 (1990).
9. J. B. Adams, M. O. Smith, and A. R. Gillespie, "Simple models for complex natural surfaces: a strategy for hyperspectral era of remote sensing," in *Proc. IEEE International Geoscience and Remote Sensing Symp.* **89**, pp. 16–21 (1989).
10. S. Tompkins, J. F. Mustard, C. M. Pieters, and D. W. Forsyth, "Optimization of targets for spectral mixture analysis," *Remote Sens. Environ.* **59**, 472–489 (1997).
11. J. W. Boardman, "Inversion of imaging spectrometry data using singular value decomposition," in *Proc. IEEE Symp. Geoscience and Remote Sensing*, pp. 2069–2072 (1989).
12. J. J. Settle and N. A. Drake, "Linear mixing and estimation of ground cover proportions," *Int. J. Remote Sens.* **14**, 1159–1177 (1993).
13. Y. E. Shimabukuro and J. A. Smith, "The least-squares mixing models to generate fraction images derived from remote sensing multispectral data," *IEEE Trans. Geosci. Remote Sens.* **29**, 16–20 (1991).
14. M. O. Smith, D. A. Roberts, J. Hill, W. Mehl, B. Hosgood, J. Verdebout, G. Schmuck, C. Koechler, and J. B. Adams, "A new approach to quantifying abundances of materials in multispectral images," in *Proc. IEEE International Geoscience and Remote Sensing Symp.* '94, pp. 2372–2374, Pasadena, CA (1994).
15. J. W. Boardman, "Leveraging the high dimensionality of AVIRIS data for improved sub-pixel target unmixing and rejection of false positive: mixture tuned matched filtering," in *Summaries of Seventh Annual JPL Earth Science Workshop*, p. 1 JPL Publication 98-4 (1998).
16. D. E. Sabol, J. B. Adams, and M. O. Smith, "Quantitative sub-pixel spectral detection of targets in multispectral images," *J. Geophys. Res.* **97**, 2659–2672 (1992).
17. E. A. Ashton and A. Schaum, "Algorithms for the detection of sub-pixel targets in multispectral imagery," *Photogramm. Eng. Remote Sens.* **64**, 723–731 (1998).
18. J. C. Harsanyi, "Detection and classification of subpixel spectral signatures in hyperspectral image sequences," PhD Dissertation, Dept. of Electrical Engineering, Univ. of Maryland Baltimore County, Baltimore, MD (1993).
19. J. C. Harsanyi, W. Farrand, and C.-I Chang, "Detection of subpixel spectral signatures in hyperspectral image sequences," in *Annual Meeting, Proc. American Society of Photogrammetry & Remote Sensing*, pp. 236–247, Reno (1994).
20. W. Farrand and J. C. Harsanyi, "Mapping the distribution of mine tailing in the Coeur d'Alene River valley, Idaho, through the use of constrained energy minimization technique," *Remote Sens. Environ.* **59**, 64–76 (1997).
21. O. L. Frost III, "An algorithm for linearly constrained adaptive array processing," *Proc. IEEE* **60**, 926–935 (1972).
22. B. D. Van Veen and K. M. Buckley, "Beamforming: a versatile approach to spatial filtering," *IEEE ASSP Mag.*, pp. 4–24 (Apr. 1988).
23. S. Haykin, *Adaptive Filter Theory*, 3rd ed., Prentice-Hall (1996).
24. L. L. Scharf, *Statistical Signal Processing*, Addison-Wesley, Reading, MA (1991).
25. C.-I Chang, X. Zhao, and M. L. G. Althouse, "Least squares subspace projection approach to mixed pixel classification in hyperspectral images," *IEEE Trans. Geosci. Remote Sens.* **36**, 898–912 (1998).
26. C.-I Chang and H. Ren, "Linearly constrained minimum variance beamforming for target detection and classification in hyperspectral imagery," in *International Geoscience and Remote Sensing Symp.* '99, pp. 1241–1243, Hamburg, Germany (1999).

27. J. C. Harsanyi and C.-I Chang, "Hyperspectral image classification and dimensionality reduction: an orthogonal subspace projection," *IEEE Trans. Geosci. Remote Sens.* **32**, 779–785 (1994).
28. C.-I Chang and C. Brumbley, "Linear unmixing Kalman filtering approach to signature abundance detection, signature estimation and subpixel classification for remotely sensed images," *IEEE Trans. Aerosp. Electron. Syst.* **37**, 319–330 (1999).
29. C.-I Chang, Q. Du, T. S. Sun, and M. L. G. Althouse, "A joint band prioritization and band decorrelation approach to band selection for hyperspectral image classification," *IEEE Trans. Geosci. Remote Sens.* **37**, 2631–2641 (1999).
30. C.-I Chang, "An information theoretic-based measure for spectral similarity and discriminability," in *International Geoscience and Remote Sensing Symp.* '99, pp. 509–511, Hamburg, Germany (1999).
31. C.-I Chang, "An information theoretic-based approach to spectral variability, similarity and discriminability for hyperspectral image analysis," *IEEE Trans. Inf. Theory* **46**, 1927–1932 (2000).
32. S. Kullback, *Information Theory and Statistics*, Dover (1968).
33. H. Ren and C.-I Chang, "A generalized orthogonal subspace projection approach to unsupervised multispectral image classification," in *Image and Signal Processing for Remote Sensing IV, Proc. SPIE* **3500**, 42–53 (1998).
34. C.-I Chang and D. Heinz, "Subpixel spectral detection for remotely sensed images," *IEEE Trans. Geosci. Remote Sens.* **38**, 1144–1159 (2000).



Hsuan Ren received the BS degree in electrical engineering from the National Taiwan University, Taipei, Taiwan, R.O.C., in 1994, and the MS and PhD degrees in electrical engineering from University of Maryland Baltimore County, Maryland, in 1998 and 2000, respectively. He received the third prize in the student paper prize competition at the 2000 IEEE International Geoscience and Remote Sensing Symposium. He is currently on a National Research Council (NRC) postdoctoral fellowship sponsored by Biological and Chemical Command, US Army, Edgewood Chemical Biological Center at Aberdeen Proving Ground. His research interests include data compression, signal and image processing, and pattern recognition. He is a member of the IEEE and Phi Kappa Phi.



Chein-I Chang received the BS degree from Soochow University, Taipei, Taiwan, in 1973, the MS degree from the Institute of Mathematics at National Tsing Hua University, Hsinchu, Taiwan, in 1975, and the MA degree from the State University of New York at Stony Brook in 1977, all in mathematics. He also received the MS and MSEE degrees from the University of Illinois at Urbana-Champaign in 1982, and the PhD degree in electrical engineering from the University of Maryland, College Park, in 1987. Dr. Chang has been with the University of Maryland Baltimore County since 1987, as a visiting assistant professor from January 1987 to August 1987, an assistant professor from 1987 to 1993, and an associate professor in the Department of Computer Science from 1993 to the present. He was a visiting research specialist at the Institute of Information Engineering at the National Cheng Kung University, Taiwan, from 1994 to 1995. He has a patent on automatic pattern recognition and several pending patents on image-processing techniques for hyperspectral imaging and detection of microcalcifications. He is currently on the editorial board of the *Journal of High Speed Networks* and is the guest editor of a special issue of that journal on telemedicine and applications. His research interests include automatic target recognition, multispectral and hyperspectral image processing, medical imaging, information theory and coding, signal detection and estimation, and neural networks. Dr. Chang is a senior member of the IEEE and a member of SPIE, INNS, Phi Kappa Phi, and Eta Kappa Nu.